Available online at www.sciencedirect.com

SciVerse ScienceDirect

Acta Materialia 59 (2011) 7340–7355

Acta MATERIALIA

www.elsevier.com/locate/actamat

Superior fatigue crack growth resistance, irreversibility, and fatigue crack growth–microstructure relationship of nanocrystalline alloys

Michael D. Sangid [a], Garrett J. Pataky [a], Huseyin Sehitoglu [a,*], Richard G. Rateick [b], Thomas Niendorf [c], Hans J. Maier [c]

[a] Department of Mechanical Science and Engineering, University of Illinois at Urbana-Champaign, 1206 West Green Street, Urbana, IL 61801, USA
[b] Honeywell Aerospace, 3520 Westmoor Street, South Bend, IN 46628, USA
[c] Lehrstuhl für Werkstoffkunde, University of Paderborn, 33095 Paderborn, Germany

Received 25 May 2011; received in revised form 27 July 2011; accepted 27 July 2011
Available online 23 September 2011

Abstract

While previous studies have reported that nanocrystalline materials exhibit poor resistance to fatigue crack growth (FCG), the electro-deposited nanocrystalline Ni–Co alloys tested in this paper show superior resistance to FCG. The high damage tolerance of our alloy is attributed to the following: alloying with Co, low internal stresses resulting in stability of the microstructure, and a combination of high strength and ductility. The high density of grain boundaries interact with the dislocations emitted from the crack tip, which impedes FCG, as predicted by the present model and measured experimentally by digital image correlation. Further, the addition of Co increases the strength of the material by refining the grain size, reducing the fraction of low angle grain boundaries, and reducing the stacking fault energy of the material, thereby increasing the prevalence of twinning. The microstructure is stabilized by minimizing the internal stress during a stress relief heat treatment following the electro-deposition process. As a result grain growth does not occur during deformation, leaving dislocation-mediated plasticity as the primary deformation mechanism. The low internal stresses and nanoscale twins preserve the ductility of the material, thereby reaching a balance between strength and ductility, which results in a superior resistance to FCG.

Keywords: Nanocrystalline alloys; Fatigue; Crack propagation; Irreversibility; Grain boundaries

1. Introduction

Nanocrystalline (NC) metals and alloys have drawn significant interest in recent years due to their high strength [1–5] and resistance to wear and extreme environments [5]. Before these materials can be widely used in engineering applications we must address their damage tolerance, specifically fatigue crack propagation (FCP). In 2003 Hanlon et al. first showed that a refinement in grain size led to increased resistance to stress controlled fatigue, although this improvement was at the expense of fatigue crack growth (FCG) resistance [6]. In this paper we will explore the FCG properties of nanocrystalline materials and show evidence of superior resistance to FCG, through NC microstructure design via alloying, a stress relief heat treatment, and grain stability to achieve a balance of strength and ductility.

In certain aspects the FCG mechanisms in NC material are similar to those reported in the classical literature on coarse grained (CG) materials. NC materials display a strong degree of work hardening, due primarily to dislocation-mediated plasticity [7]. As a consequence, both fatigue striations [8,9] and shear bands [8,10] have been observed in NC fatigued materials. Using atomic force microscopy (AFM) Xie et al. measured the striation spacing and associated shear band width, both of which increased with

* Corresponding author. Tel.: +1 217 333 4112; fax: +1 217 244 6534.
E-mail address: huseyin@illinois.edu (H. Sehitoglu).

1359-6454/$36.00
doi:10.1016/j.actamat.2011.07.058

crack size [8]. In their words, the crack tip is dominated by dislocation-mediated deformation in the form of shear bands [8], which conforms to the classical mechanism of FCG in CG materials. From a continuum standpoint, the faster FCG rate of NC materials can be attributed to a less tortuous path, i.e. very straight cracks [8,11]. At low stress intensity ranges ΔK, near threshold, flat non-tortuous cracks were observed, which transitioned to a combination of fatigue striations and dimples on the fracture surface at mid ΔK, and at overload (high ΔK) the fracture surface was dominated by ductile dimples [12]. Additionally, the mechanisms active for crack shielding and plasticity/roughness-induced crack closure are expected to be lower for NC materials [4], further reducing the FCG resistance. Hence, from a continuum point of view, many of the crack propagation mechanisms are similar in NC and CG materials.

To truly understand FCG in NC materials we must note the unique deformation mechanisms of NC materials, which differ from CG materials, including disintegration of dislocation pile-ups and the prevalence of twinning [2]. In the early stages of fatigue the material exhibits cyclic hardening, which may be due to dislocation source exhaustion followed by irreversible grain boundary (GB) processes, sliding, and diffusion [13,14]. The deformation in NC fatigue specimens was due to dislocation emission at the GB, intragranular slip, and unaccommodated GB sliding; the combination of these mechanisms leads to void nucleation at GB and triple points, which results in dimple rupture with dimples significantly larger than the grain size [7]. Focused ion beam analysis showed that the mechanism for crack advancement is nanovoid coalescence ahead of the crack tip [12].

Typically steady-state FCG is thought to be almost microstructure independent, although in NC materials the microstructure, specifically the GB, plays a distinct role and is paramount in the deformation and fracture behavior [5]. The GB microstructure strongly affects the fatigue response of the material, as demonstrated in a NC Ni alloy, which displayed a high fraction of low angle GB (LAGB) and twins resulting in a higher fatigue endurance stress than conventional polycrystalline Ni materials [15]. Cavaliere has observed dislocation-based slip bands emanating from the crack tip in NC pure metals (Al, Ti, Ni, and Cu), which were stopped at high resistance GB [16]. In some cases the grains ahead of the crack tip rotated to form LAGB (grain coalescence) to assist in dislocation-mediated plasticity [10]. Some of the microstructural features that influence FCG are depicted in Fig. 1.

As proposed by Rice and Thomson, at the crack tip there is competition between crack blunting (i.e. dislocation nucleation) and crack advancement [17]. Ovid'ko and Sheinerman [18] discussed crack blunting by a GB creep mechanism (originally proposed by Wei et al. [10]) in NC materials, whereas crack advancement is enabled by GB decohesion. Hence, as dislocations are emitted from the crack tip and pile-up at an adjacent GB there exists a critical number of dislocations before emission of further dislocations is inhibited by the stress field associated with the existing pile-up [18,19]. Additionally, in NC materials this behavior is complicated by the evolving microstructure, as there is stress-driven migration/sliding of GB, which affects crack growth. Hence, the evolving microstructure attributed to the fabrication techniques must be noted.

There are many different methods to fabricate NC materials, as described elsewhere [2]. In this study we focus on electro-deposition (ED) fabricated Ni–Co alloys due to their low investment, alloy/grain size control, and relatively high production rates (compared with other NC manufacturing processes). In ED NC Ni–Co alloys, the grain size and twin density can be fine tuned based on the process controls as annealing twins form readily during deposition [20]. However, the grain morphology and size are also influenced by the Co content in the alloy [21]. Additionally, there is batch to batch variation, which makes it difficult to ascertain structure–property causation. In other words, a wide distribution of grain sizes in ED NC materials exists and it is difficult to determine which segment of the distribution dominates the overall material response [5]. To add complexity to the problem at hand, simple characterization such as grain size, texture, and twin density is difficult to measure in NC materials and is often not reported in individual studies, thus making it hard to quantitatively compare results [5]. The majority of the NC literature reported inferior FCG resistance (for instance ED Ni, average grain size 30–50 nm, [5–7,11,13]) with only one study reporting superior FCG properties [22]. Based on the fabrication, the microstructure of NC metals and alloys may be far from equilibrium and therefore unstable [1,3]. During fatigue testing ED NC alloys can display signs of grain growth [15] and possible creep deformation at room temperature [2,13]. Thus the stability of the microstructure and its associated evolution during fatigue testing must be taken into account when analyzing the FCG behavior of NC materials.

To enhance the damage tolerance response of NC materials there must be a compromise between strength and ductility, and this has been the aim of sustained research efforts. In metals and alloys strengthening mechanisms typically block dislocation motion. NC materials have excellent strength at the expense of ductility. Thus the goal is to promote strength while preserving ductility by the following: coherency with the surrounding matrix, thermal/mechanical stability, and small (nanoscale) features. One such feature is nanoscale twin boundaries [23]. In this paper we characterize the microstructure of a NC ED Ni–Co alloy that displays superior FCG resistance compared with CG materials. This is accomplished by a high twin volume fraction, small grain size, and a stress relief heat treatment that enhances ductility and stabilizes the GB structure. The deformation and FCG results are systematically analyzed using digital image correlation (DIC), scanning electron microscopy (SEM), and transmission electron microscopy (TEM) in order to explain the

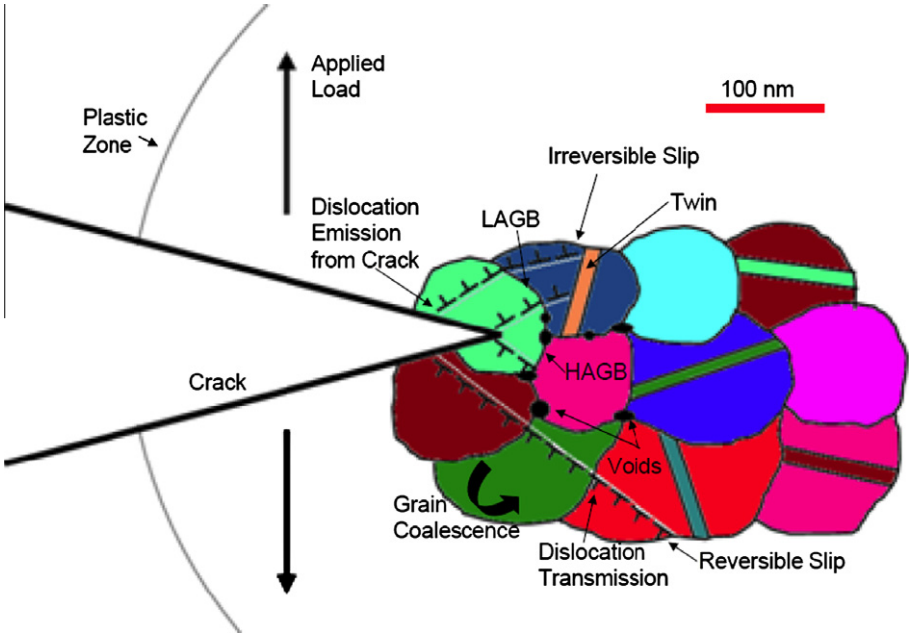

Fig. 1. Schematic of FCG through a NC material indicating that the material microstructure plays a significant role in the rate of crack propagation. At the crack tip there is competition between dislocation emission and crack propagation, which is influenced by the microstructure. HAGB and twins block dislocations, while LAGB and grain coalescence, where grains rotate to form LAGB, allow dislocations to transmit across GB.

fatigue irreversibility and damage resistance of this material. Finally, we introduce a model of dislocation-mediated plasticity at the crack tip to shed light on the observed microstructure-sensitive enhanced FCG resistance.

2. Material characterization and experimental methods

2.1. Material characterization

The material studied is ED Ni–Co alloy sheets from sulfamate-based solutions manufactured by NiCoForm Inc. Ni–Co alloys have higher strength and hardness compared with pure Ni, thus piquing interest in studying this alloy. Three compositions of the alloy were fabricated at the same current density with cobalt contents by weight of 1.0%, 1.62%, and 5.52%, with the balance being nickel. Extreme care was taken to minimize the internal stress within the material during ED, as this provides a balance between strength and ductility of the alloy [http://www.nicoform.com/files/upload/upload/23/Mechanical.pdf 2010].

The alloy sheets were 0.12 mm thick and 152.4 mm × 152.4 mm. After ED the specimens were heat treated at 250 °C for 1 h. This is considered a stress relief process as the grain structure does not coarsen, but becomes more compact [http://www.nicoform.com/files/upload/upload/23/Mechanical.pdf 2010]. Hence, the microstructure stabilizes and a compromise is reached between size, strength, and ductility. Tensile specimens were cut from the sheets with the gage section of 14 mm long, 3 mm wide, and 0.12 mm thick. For FCG experiments a single electro-discharge machined edge notch 0.5 mm deep was added to the specimens using a 0.152 mm diameter wire.

Using high resolution electron back-scattering diffraction (EBSD) the textures of the Ni–Co alloys were measured. Fig. 2 displays orientation maps of the three compositions of the alloy. From the EBSD maps it appears that the material displays a slight ⟨1 0 1⟩ texture, although the Taylor factor calculation results in a value of 3.06 under uniaxial loading (random texture for fcc materials), indicating that the material does not display a preferential texture.

For this NC alloy the grain size approaches the resolution of the EBSD system and thus the data were filtered through a dilation process removing points with a confidence index standardization less than 0.2. During the EBSD scan the material is probed about a grid with a step size of 50 nm to obtain the orientation of the material at each point in the grid. If the misorientation between two points is greater than 2° the EBSD software places a GB in between the two points. It is possible that very small grains, which are difficult to detect given the resolution and a step size approaching the grain size of the material, are not properly detected. Fig. 3 shows the grain size distribution for the Ni–1% Co FCG specimen. Note that this distribution is therefore an upper bound due to the resolution limit of the EBSD. The grain sizes were validated through TEM images, although TEM cannot be used to report reliable size statistics and distributions due to the small sample area probed.

On inspection the Ni–1% Co specimens appear to have coarser grains with more LAGB, while the Ni–5.52% Co specimens have finer grains with more high angle grain boundaries (HAGB). The Ni–1.62% Co specimens represent a median between these two extremes. Hence, a higher

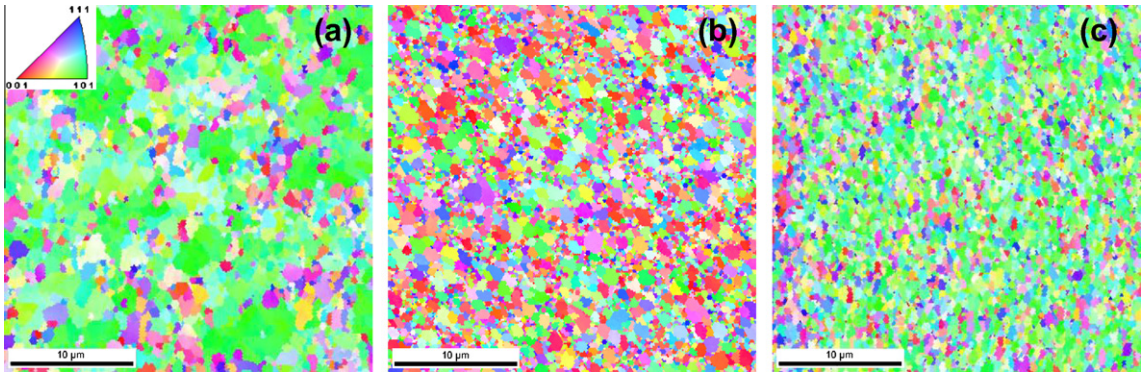

Fig. 2. EBSD scans displaying orientation maps for specimens with the following ED NC compositions: (a) Ni–1% Co; (b) Ni–1.62% Co; (c) Ni–5.52% Co. Due to the grain size approaching the resolution of the EBSD system the data were filtered and cleaned using grain confidence index standardization.

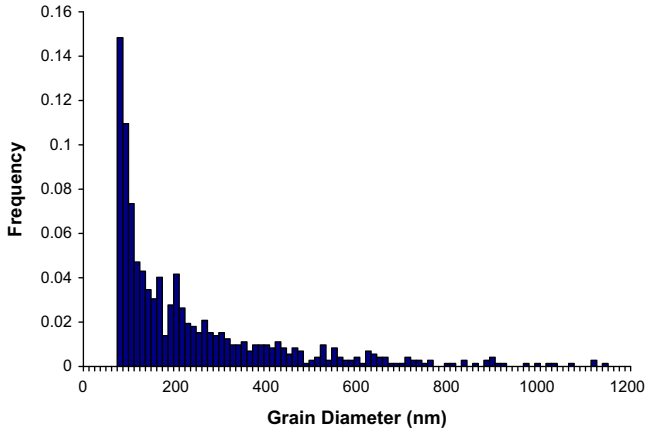

Fig. 3. Grain size distribution for the Ni–1% Co FCG specimen measured using high resolution EBSD (filtered and cleaned using grain confidence index standardization). The contribution of small grains (less than 75 nm in diameter) to the data may have been affected by the filtering, hence this distribution should be taken as an upper bound.

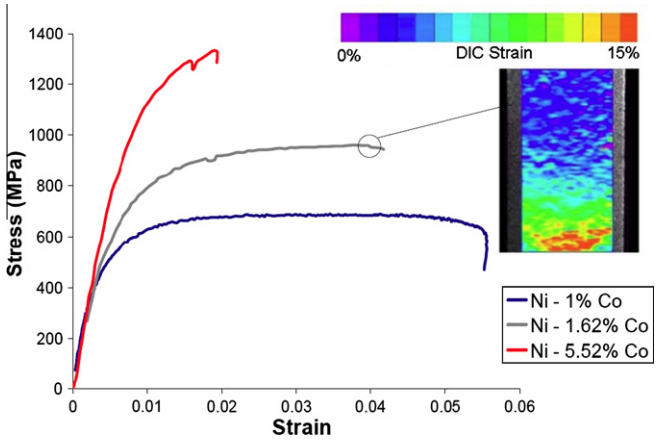

Fig. 4. Monotonic tensile test results for three compositions of ED NC Ni–Co alloy. The inset shows the strain fields in the Ni–1.62% Co specimen determined by DIC, where the largest local strains reached 15% prior to failure.

content of Co refines the grain size in the specimens and leads to a larger misorientation in the GB population. Statistical analysis of the EBSD specimens reveals a high content of twins and LAGB, nearly 40% and 20%, respectively, in the Ni–1% Co, although, as previously mentioned, the accuracy of these values may be compromised due to the limit of resolution of the EBSD system. The role of grain size and twins in the mechanical response of this alloy is discussed in greater detail in Sections 4.1 and 4.5, respectively.

Table 1
Tensile properties for the three Ni–Co alloys with different chemistries.

	E (GPa)	σ_y (MPa) 0.2% Offset	UTS (MPa)	Elongation (%)
Ni–1% Co	180	522	689	5.6
Ni–1.62% Co	159	631	961	4.2
Ni–5.52% Co	165	1020	1332	1.9

2.2. Experimental methods

Monotonic tension and FCG experiments were conducted in air at room temperature. The cracks grew horizontally through the specimens as the applied cyclic loading was normal to the cracks, thus indicating mode I crack growth. FCG experiments were performed using a triangular waveform with a cyclic frequency of 5 Hz at a load ratio of 0.05 until a crack initiated. Stress ranges of 213.75–225, 190–200, and 261.25–275 MPa were used to cycle the Ni–1.0% Co, Ni–1.62% Co, and Ni–5.52% Co specimens, respectively. Once a crack had initiated measurement cycles of 0.25 or 0.50 Hz were run every 500–1000 cycles to capture data for DIC analysis.

DIC has recently begun to be used to analyze FCG in order to understand both global and local phenomena. For a detailed explanation of the methodology behind DIC see Sutton et al. [24]. Recording load and image information simultaneously, DIC has been used in situ to give an in-depth look into fatigue cycles with established methods [25,26].

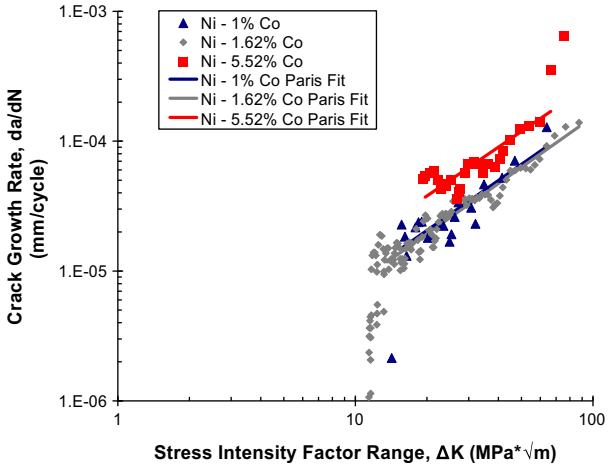

Fig. 5. FCG results for Ni–Co of various compositions. The tests were completed at room temperature in air with a stress ratio value of $R = 0.05$. The data points are shown for the complete FCG results, while the Paris line fits are only displayed for region II. The Paris law coefficients and threshold stress intensity factor ranges are shown in Table 2.

Table 2
Fatigue crack growth Paris law coefficients and threshold stress intensity factor range values for three Ni–Co alloys with different chemistries.

	$\Delta K_{threshold}$	C	m
Ni–1% Co	14 MPa $*$ $\sqrt{m}$	4.44×10^{-7}	1.28
Ni–1.62% Co	11.4 MPa $*$ $\sqrt{m}$	4.05×10^{-7}	1.29
Ni–5.52% Co	18 MPa $*$ $\sqrt{m}$	8.95×10^{-7}	1.25

The specimens used during testing were mechanically polished to a mirror finish. A speckle pattern was then air-brushed onto the specimens using black paint. Correlations were performed using a maximum subset size of 130 μm × 130 μm at a step size of 30 μm. For the FCG experiments the pixel sizes were 1.58, 1.7, and 1.25 μm for the Ni–1.0% Co, Ni–1.62% Co, and Ni–5.52% Co specimens, respectively.

3. Results

3.1. Monotonic tensile tests

The stress–strain results for the three compositions of ED NC Ni–Co alloys, Ni–1.0% Co, Ni–1.62% Co, and Ni–5.52% Co, are shown in Fig. 4. The tensile properties for each alloy are summarized in Table 1. It can be seen that all three alloys have nearly the same elastic modulus, as expected. The Ni–5.52% Co material has the highest yield strength, hardening, and ultimate tensile strength, although the percent elongation and, consequentially, its ductility is lowest amongst the three alloys. In fact, the strength and hardening rate of the Ni–5.52% Co are remarkably high, with yield and tensile strengths of 1.02 and 1.33 GPa, respectively, but at the expense of ductility. The Ni–1.0% Co material has the lowest yield strength, hardening, and tensile strength, but its elongation and ductility are highest at 5.6%. Furthermore, the lower percentage of Co gives the material an almost flat, perfectly plastic secondary hardening behavior after the initial hardening post-yielding. The Ni–1.62% Co material presents a median compromise between strength and ductility compared with the higher and lower weight percentages of Co. Additionally, the DIC axial strain field is shown for the Ni–1.62% Co specimen immediately before failure in the inset to Fig. 4. It can be seen that the local strains that accumulate in the specimen are nearly 15%, while the nominal strain is approximately 4%. This indicates that the material is relatively ductile in the vicinity of damage accumulation.

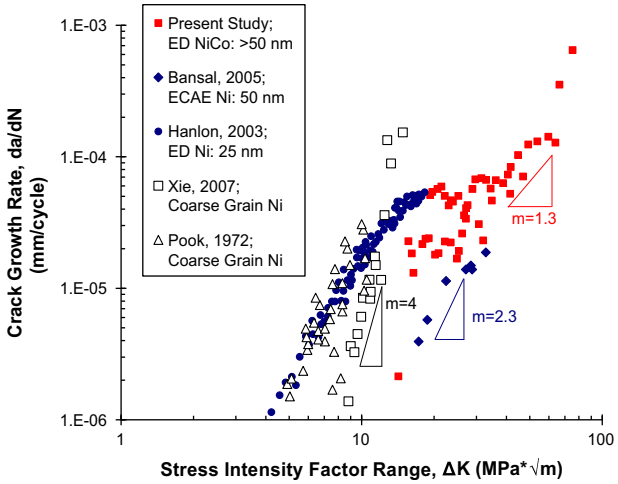

Fig. 6. FCGR for all three compositions of ED NC Ni–Co (red squares) are compared with data from the literature for coarse grained Ni (black outlined points) and nanocrystalline Ni (solid blue points). It can be seen that the data in this study have a lower Paris law coefficient m (slope), indicating that the heat-treated Ni–Co material shows better crack propagation resistance compared with coarse grained (not as strong) or nanocrystalline (not as ductile) Ni.

3.2. Fatigue crack growth tests

The FCG results for the three compositions of Ni–Co are shown in Fig. 5. The Ni–5.52% Co specimen displays a slightly faster FCG rate (FCGR) compared with the Ni–1.0% Co and Ni–1.62% Co specimens, which show nearly the same FCGR. The large amount of scatter seen in the tests is indicative of the resolution of the DIC images, which were used to record the incremental crack growth rates da and the crack lengths a, to calculate the values of da/dN and ΔK in Fig. 5:

$$\Delta K = F \cdot \Delta\sigma\sqrt{\pi a}, \tag{1}$$

where $\Delta\sigma$ is the applied stress range and F is the geometric correction factor [25]. Most of the points captured by DIC imaging are contained in region II of the FCG curve. A power law, Paris equation regression can be fitted to each curve, as shown by the straight solid lines in Fig. 5.

$$\frac{da}{dN} = C(\Delta K)^m. \tag{2}$$

The coefficients for the Paris law (C and m), along with the threshold stress intensity factor range ΔK_{th} value (for which cracks start to grow), are shown in Table 2. It can be seen that the Paris law exponent m is roughly constant for each of the three specimens at 1.25–1.29. Further, this value of the Paris law exponent is considerably smaller than typical values for engineering alloys, which are in the range $m \approx 2$–7 [27] and typically $m = 3$ or 4. This indicates that the ED NC Ni–Co material exhibits a greater resistance to FCP then typical engineering alloys.

A comparison of the ED NC Ni–Co in the present study with other values for pure nickel in the literature is shown in Fig. 6. All three compositions of ED NC Ni–Co are plotted together using the red solid squares, hence the large degree of scatter in these results can be attributed to the three separate specimen conditions. The Paris law exponent m of the ED NC Ni–Co is approximately 1.3. Hence ED NC Ni–Co displays slower FCGR compared with typical CG Ni (black outlined squares [8] or black outlined triangles [28]), which exhibited a Paris law exponent m of approximately 4. Furthermore, ED NC Ni–Co displays slower crack growth rates compared with NC Ni from ECAE (blue solid diamonds) [22] or ED (blue solid circles) [6], which displayed a Paris law exponent m of 2.3. Each of the NC Ni materials in the literature represents pure Ni in a non-heat-treated condition with a finer grain size (50 and 25 nm, respectively) compared with the material in the present study (for grain size distributions see Fig. 3).

During the fatigue tests, the displacement fields of the specimens were recorded using digital image correlation. As previously indicated, the cracks grew through a mode I opening mechanism, thus only the vertical displacements v were evaluated and regressed using the equation:

$$v = \frac{K_I}{\mu}\sqrt{\frac{r}{2\pi}}\sin\left(\frac{\theta}{2}\right)\left[\frac{1}{2}\left(\left(\frac{3-\upsilon}{1+\upsilon}\right)+1\right)-\cos\left(\frac{\theta}{2}\right)\right] - \frac{1}{2\mu}\left(\frac{\upsilon}{1+\upsilon}\right)Tr\sin(\theta)+Ar\cos(\theta)+B, \quad (3)$$

where r is the distance from the crack tip, θ is the angle to the crack, μ is the shear modulus, and υ is the Poisson ratio. In order to calculate values for K_I, the stress intensity

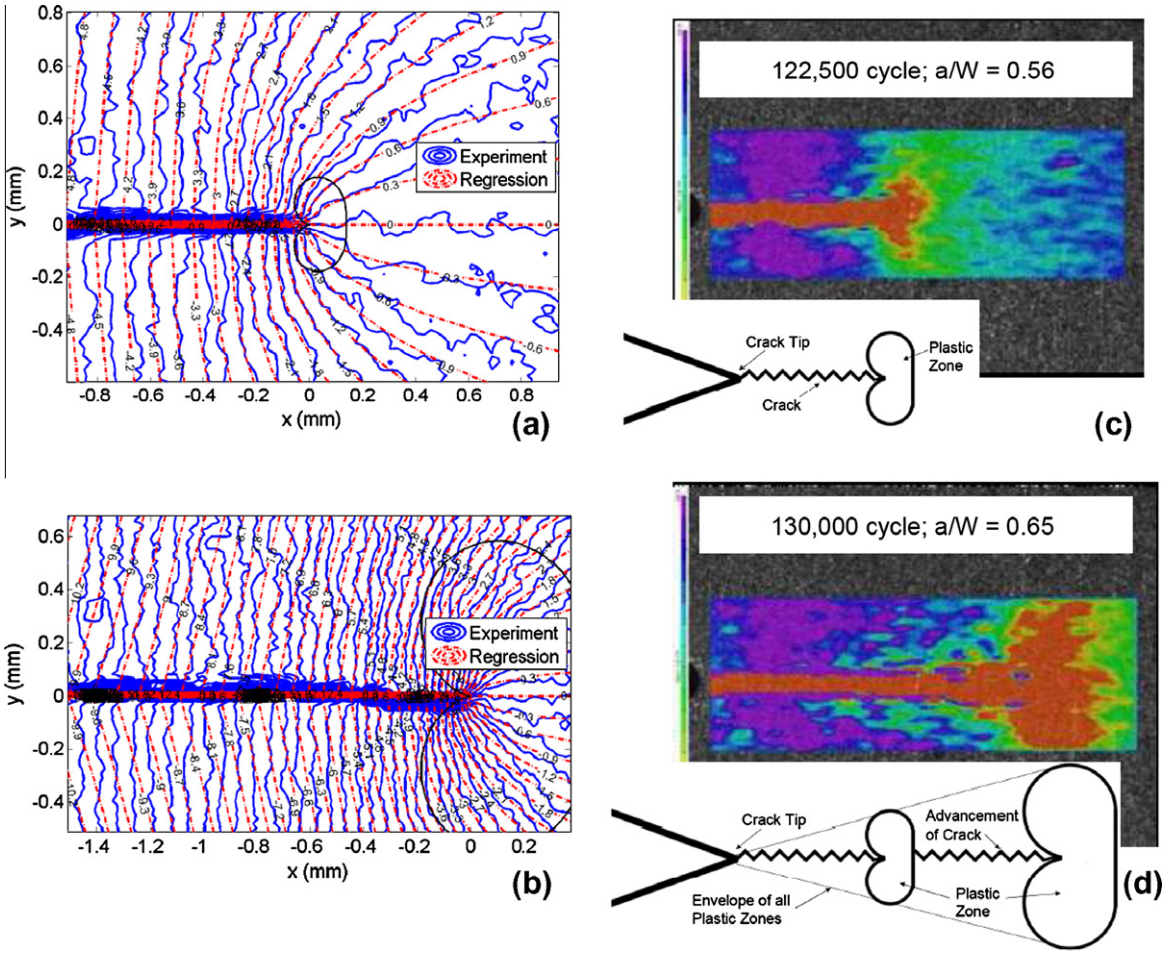

Fig. 7. DIC measurements of crack advance during $R = 0.05$, $\sigma_{max} = 200$ MPa loading of the Ni–1.62% Co alloy. Vertical displacement contours (μm) with regression curves and plastic zones ahead of the crack tip for (a) 122,500 and (b) 130,000 maximum load cycles. (c) Observations of strains in the vicinity of the crack tip, where the plastic strains are shown in red with schematics of the plastic zone envelope shown in the insets for (c) 122,500 and (d) 130,000 cycles.

factor, T, the T-stress representing the uniform stress component parallel to the crack, A, the rigid body rotation, and B, the rigid body translation, are included in the calculation. Figs. 7a and b show the calculated K_I for 122,500 and 130,000 loading cycles. The plastic zone ahead of the crack tip is also determined based on the stress intensity factor found in the regression of Eq. (3) using Westergaard's solution for stress fields around a crack tip [29] assuming the Von Mises criterion for yielding and plane stress conditions. As expected, as the crack advances the plastic zone ahead of the crack tip expands. Further, we can compare the strain fields ahead of the crack tip (Fig. 7c and d) to the yield locus (Fig. 7a and b). Progression of the plastic zones can be seen in Fig. 7d during crack advancement via the strain fields, thus replicating the envelope of all plastic zones (in the inset), which was originally illustrated by Elber [30].

3.3. Plasticity-induced crack closure

During FCG, knowledge of the actual cyclic load range is the key to understanding the effective cyclic displacements at the crack tip. The full applied load range is not always experienced by the crack tip as the crack tip may close, i.e. displacements cease prior to the minimum load. In other words, the crack tip may be shielded from the effects of part of the load cycle, which is commonly referred to as crack closure. Roughness-induced crack closure was observed by Christensen [31], while plasticity-induced crack closure was observed by Elber [32]. The significance of crack closure is that it acts as a shielding mechanism for load, which reduces the effective stress intensity factor range at the crack tip:

$$\Delta K_{\text{eff}} = K_{\max} - K_{\text{open}}. \tag{4}$$

Thus the effective stress intensity factor range ΔK_{eff} only accounts for the portion of the stress intensity factor range above the crack opening level K_{open}. The full field displacement measurements for DIC account for the material behavior in the vicinity near the crack, but also at the crack tip. Thus the K_I values obtained by the regression in Eq. (3) provides the effective stress intensity factor range by only accounting for the contributions of the stress intensity factor when the crack is fully open, i.e. crack tip displacements

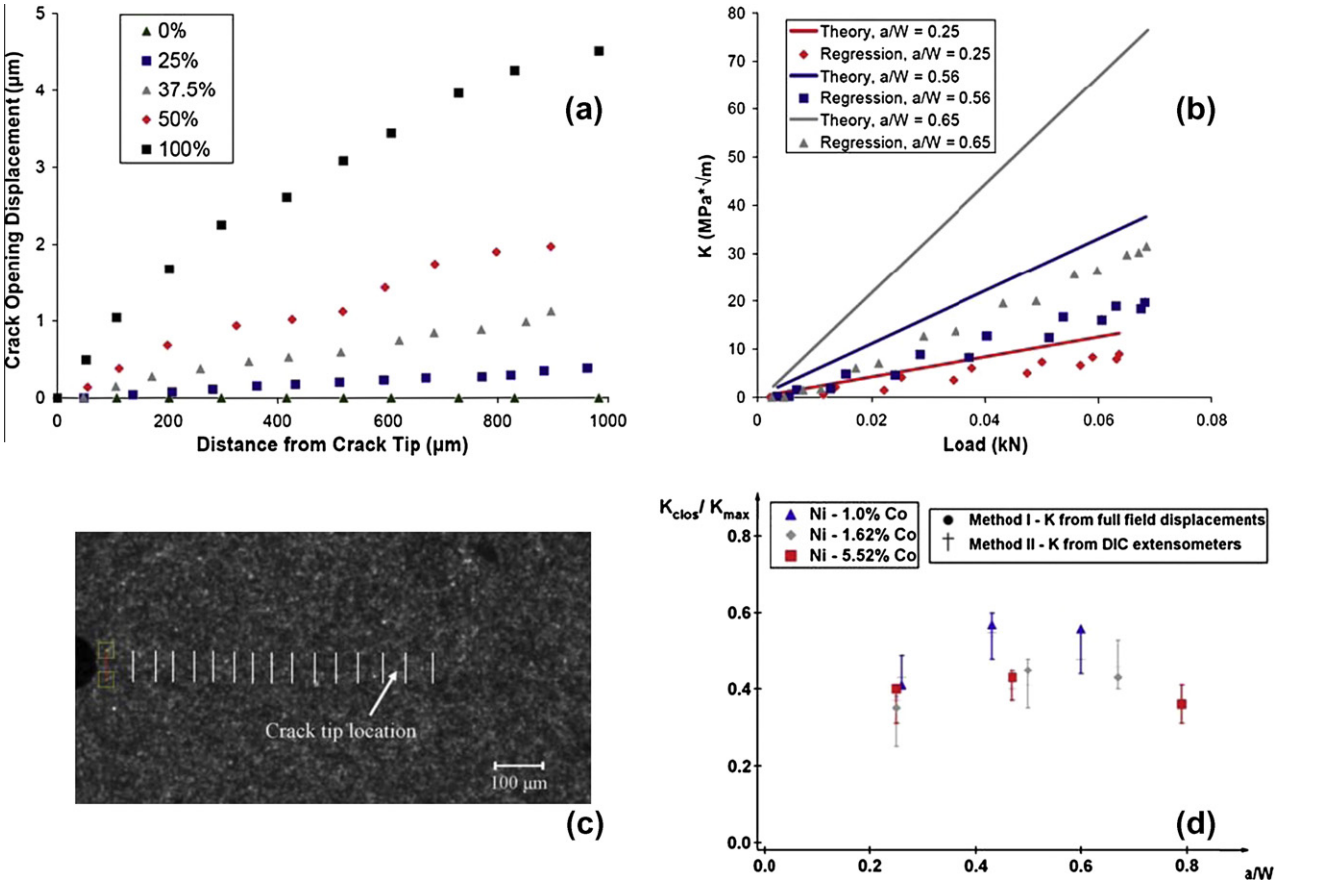

Fig. 8. (a) The profiles of the crack shown as crack opening displacement as a function of distance from the crack tip for various percentages of load during a single cycle for a Ni–1.62% Co FCG specimen determined from the DIC analysis. The crack opens between 37.5% and 50% of the maximum applied load. (b) The theoretical (solid lines) and DIC regression (data points) stress intensity factors during the loading cycle accounting for plasticity-induced crack closure for various crack lengths (a/W) of the Ni–1.62% Co FCG specimen. (c) Schematic of DIC extensometers placed at the crack flanks to measure strain. (d) Ratio of stress intensity factor values when the crack closes versus the maximum as a function of crack length for various compositions of Ni–Co alloy. Two DIC methods are used for comparison and error estimation: full field regression and extensometers.

exist. As a consequence, the regression values of the stress intensity factor range ΔK_{eff} accounting for crack closure can be compared with the theoretical values of the stress intensity factor range (Eq. (1)) during the loading cycle for various crack lengths, as shown in Fig. 8a.

In order to verify the DIC regression quantification of crack closure, DIC extensometers were placed on the crack flanks all the way to and beyond the crack tip to reproduce the crack opening displacement (Fig. 8c). During the FCG experiments the displacements at the crack tip were measured using the DIC extensometers, giving an accurate profile of the crack opening displacements during applied loading [25]. Fig. 8a shows the crack opening displacements as a function of distance from the crack tip during the loading cycle for different percentage loads. Based on the shape and length scale of the crack profile we can determine whether the crack is open or closed at prescribed loading intervals. As expected, at 0% loading the crack is completely closed. The crack remains closed at 25% and 37.5% of the maximum load as the second data point (at a distance of 50 μm from the crack tip) has zero crack opening displacement, indicating that the crack tip is shut. The crack remains closed up to 37.5% of the maximum loading; a closed crack is defined in this plot as having a crack opening displacement of zero at a prescribed distance (non-zero value) from the crack tip. Hence, in Fig. 8a the crack opens between 37.5% and 50% of the maximum load. At 50% loading and above the crack is fully open.

Thus far we have presented two methods for measuring plasticity-induced crack closure: (i) K from full field regression (Eq. (3)); (ii) K from DIC extensometers. Fig. 8d compares the crack closure values obtained by these two methods as the ratio of the stress intensity factor value at closure versus the maximum stress intensity factor and is plotted as a function of crack length (in terms of crack length a over specimen width W). It can be seen that the two methods give similar results, as the data from the regression are within the measurement error of the DIC extensometers. As previously mentioned, longer cracks have a larger degree of plasticity ahead of the crack tip, which results in greater values of plasticity-induced crack closure. This trend is seen initially in Fig. 8d, although as a/W approaches 1 the trend no longer holds. There is insufficient material in the specimen to allow for significant crack closure as the crack length approaches the width of the specimen.

As a consequence of a lower effective stress intensity factor range ΔK_{eff} (Eq. (4)), compared with ΔK, Eq. (2) is modified, thereby reducing the crack growth rate [30] as follows:

$$\frac{da}{dN} = C'(\Delta K_{eff})^{m'}. \quad (5)$$

The effective FCG results on modifying for crack closure are shown in Fig. 9 and the modified Paris law coefficients C' and m' are shown in Table 3. Note the data shift to the left as the stress intensity factor range is reduced according to Eq. (4). Thus the threshold values are smaller, as shown in Table 3, and as a result a smaller crack can start to grow at the same applied stress range or, in other words, a crack can grow under a smaller applied stress range.

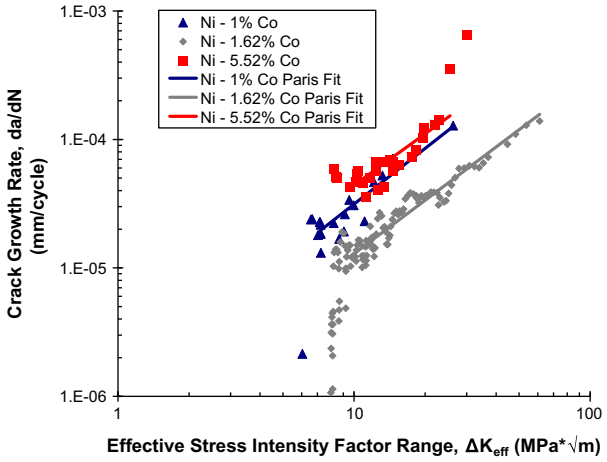

Fig. 9. Effective FCG results for ED NC Ni–Co for various compositions taking into account crack closure. The data points are shown for the complete FCG results, while the Paris line fits are only displayed for region II. The effective Paris law coefficients and threshold stress intensity factor ranges are shown in Table 3.

Table 3
Fatigue crack growth effective Paris law coefficients and threshold stress intensity factor range values for three Ni–Co alloys with different chemistries. The values are modified from Table 2 by including the effects of plasticity-induced crack closure on fatigue crack growth.

	$\Delta K_{threshold}$	C'	m'
Ni–1% Co	6 MPa $*\sqrt{m}$	1.14×10^{-6}	1.44
Ni–1.62% Co	8 MPa $*\sqrt{m}$	5.38×10^{-7}	1.38
Ni–5.52% Co	7.5 MPa $*\sqrt{m}$	2.06×10^{-6}	1.33

Note the effective crack growth exponent m' is nearly the same for all three compositions of the ED NC Ni–Co alloy, with values of 1.33–1.44. Thus this alloy offers substantial resistance to FCP compared with CG [8,28] or NC [6,22] materials reported in the literature. Additionally, once again the higher concentration of Co in the alloy, Ni–5.52% Co, shows a faster FCGR compared with the Ni–1.62% and Ni–1% Co alloys. While previously the Ni–1% Co and Ni–1.62% Co alloys exhibited similar FCG resistance (Fig. 5), the Ni–1% Co specimen displayed higher levels of crack closure compared with the Ni–1.62% Co alloy. Hence, the phenomenon of crack closure explains the discrepancy in effective FCGR between the Ni–1% Co and the Ni–1.62% Co alloys in Fig. 9.

4. Discussion

4.1. microstructure differences between Ni–Co compositions

As previously discussed in Section 3.1, the Ni–Co alloys with higher concentrations of Co showed greater strength and a stronger hardening response, as shown in Fig. 4.

The rationale for this additional strength lies in the microstructural difference between the alloys. On inspection of the EBSD orientation maps it appears that the added Co content acts as a grain refiner (Fig. 2). This is confirmed by TEM images of the microstructure, as shown in Fig. 10. As shown in Fig. 10a, the Ni–1% Co alloy has many coarse grains, which are larger than 200 nm, whereas the Ni–5.52% Co contains much finer grain sizes on average (Fig. 10b). The combination of TEM images (small area, thus not reliable for statistics) and EBSD (lower resolution due to the small grain sizes) provides evidence that the Ni–5.52% Co has a finer grain structure compared with Ni–1% Co. This refinement of grain size is in the so-called "Hall–Petch breakdown" regime, where grain size refinement still results in an increase in flow strength of the material. Unlike the classical Hall–Petch relation, the underlying mechanism is not a pile-up of dislocations, hence the $\sigma_y \propto d^{-1/2}$ relationship does not hold in this regime. Based on the refinement in grain size, an increase in strength has been observed in the literature [5], which would account for the tensile response observed in Fig. 4.

In addition to grain refinement in the higher Co content alloys, leading to a higher flow stress, another difference in microstructure results in strengthening benefits. As can be seen in Fig. 2, the Ni–1% Co has many similar colored regions within the EBSD scan. This indicates that there are grain neighbors with similar orientations resulting in LAGBs (misorientation less than 15°), whereas the alloys with higher concentrations of Co result in fewer LAGB. LAGB allow slip transmission and are not effective barriers to dislocations [33]. Hence LAGB do not have the same strengthening benefit compared with HAGB. This has been demonstrated both experimentally and numerically [34]. As a result, materials with higher fractions of LAGB have lower hardening capabilities and, consequently, lower strength. Hence the increased concentration of Co in the ED NC Ni–Co alloys resulted in a lower content of LAGB and grain refinement, which results in a more pronounced strengthening response of the material, as shown in Fig. 4.

4.2. Damage resistance

As shown in Fig. 6, the ED NC Ni–Co alloys in this study have superior resistance to FCP compared with conventional CG or other NC Ni materials (based upon the Paris law exponent m). It has been the consensus in the past literature that grain size refinement leads to detrimental FCP resistance properties [6], which is contrary to the data reported here. The purpose of this section is to explain the discrepancy in FCG results in NC materials. We will show that the improved resistance to FCG of the ED NC Ni–Co alloys in this study is a combination of alloying, stress relief heat treatment, and grain stability to achieve a balance of strength and ductility.

First, it is necessary to demarcate the mode of FCG by observing the fracture surface of the Ni–Co specimens. In Fig. 11a pre-cracking of the specimen is seen as a crack initiates from the root of the notch within the FCG specimen and propagates to the left. By studying the fatigue fracture surface (Fig. 11b) we note significant plasticity as the material has undergone a large degree of mechanical working. Additionally, there appear to be signs of the crack closing, resulting in sliding of the two halves of the fracture surface on top of each other. This further validates the plasticity-induced crack closure measurements in Section 3.3 and Fig. 8. Lastly, the fracture surface also shows signs of small pores. These pores could be the formation of voids at the GB and triple points, which form ahead of the crack tip, as indicated by Kumar et al. [7] and Yang et al. [12].

As the crack transitions from growth in region II to the unstable region III we see that the fracture surface also transitions from a fatigue area to an overload area, as shown in Fig. 11c. From this transition it is clear that the plasticity also shifts from the cross-sectional area of the specimen (which the fatigue fracture surface encompasses) to a very small necked region. If we take a closer look at the necked region we can see that the specimen cross-section of 120 μm reduces to 20 μm, which involves significant plasticity as the deformation localizes into a small grove, as

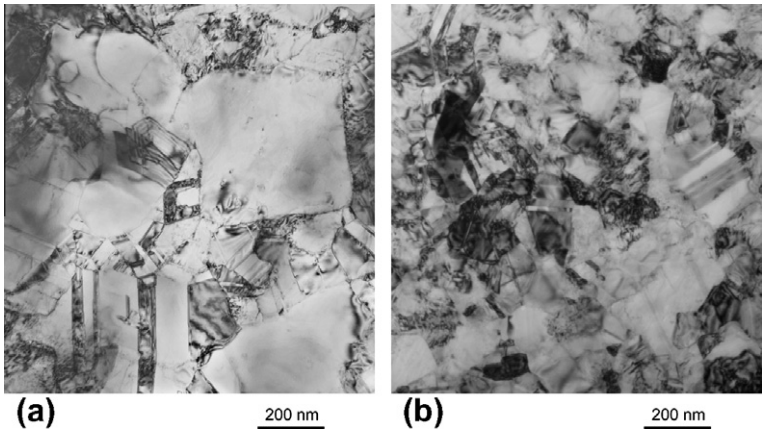

Fig. 10. Comparisons of grain size determined by TEM microscopy for two compositions of ED NC Ni–Co alloys: (a) Ni–1% Co (as-received specimen); (b) Ni–5.52% Co (as-received specimen). The addition of a larger percentage of Co acts to refine the grain size as seen in the fine grained Ni–5.52% Co compared with the coarser grained Ni–1% Co.

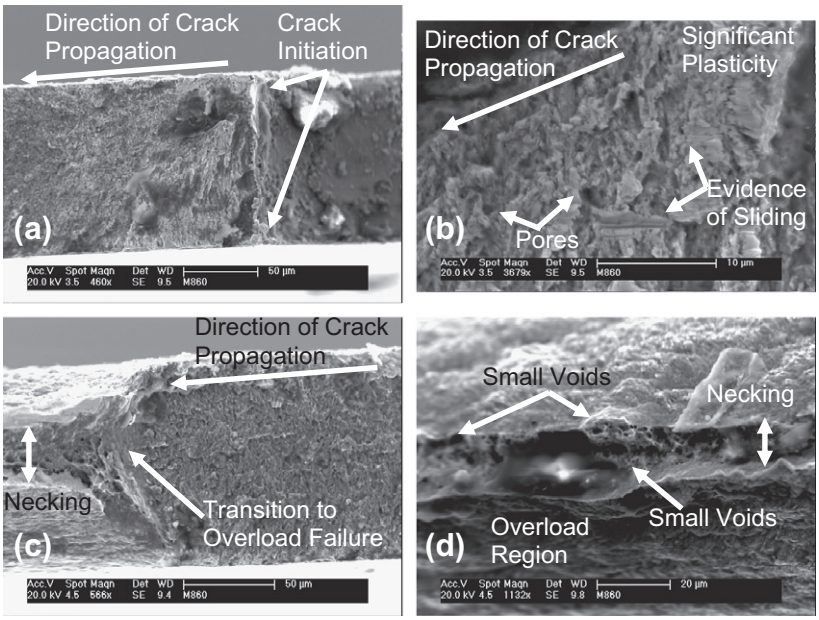

Fig. 11. Fractography (SEM images of the fracture surface) of a Ni–1.62% Co FCG specimen. (a) The location of crack initiation from the notch of the specimen as the crack propagates to the left. (b) Fatigue fractured surface as the crack moves to the lower left of the picture. Significant signs of plasticity can be seen as pores and evidence of sliding is also observed. (c) Crack transition from the fatigue fractured surface (right) to the final overload area (left). Considerable necking is seen, which is evidence of plasticity. (d) Close-up view of the necked region within the overload region. Small voids or pores are apparent at the top and within the grooves.

shown in Fig. 11d. Small voids/pores are evident at the top and base of the necked region.

By viewing the plastic zone size ahead of the crack tip during cyclic loading (Fig. 7a and b) one can see that the radius of the plastic zone is of the order of 10^{-4} m and, as previously indicated, the grain size is of the order of 10^{-7} m (Figs. 3 and 10). Therefore, we would expect thousands of grains to lie within the plastic zone or, in other words, the crack induces a plastic strain in thousands of grains during propagation. Hence our results are in agreement with other FCG studies of NC materials that suggest cyclic crack propagation is dislocation mediated and, therefore, a plastic process [7–10,15,16].

Note in Figs. 5 and 9 that the material with the least resistance to FCP is the Ni–5.52% Co. In our study this material is the strongest, albeit the least ductile, material, as indicated in Fig. 4 and Table 1. From this data we can conclude that a balance between strength and ductility is necessary for acceptable and improved FCG properties. All three alloys tested in this study exhibited substantial strength ($\sigma_y > 500$ MPa) due to the small (NC) grain size. Hence the strength is sufficient to resist crack propagation only when coupled with an adequate ductility. It can be seen that the Ni–5.52% Co has approximately 2% nominal ductility, whereas the Ni–1% Co and Ni–1.62% Co alloys both possess a nominal ductility greater than 4%. As can be seen in the inset to Fig. 4, the ED NC Ni–Co material can withstand local strains as high as 15%, which is especially important in fatigue, where high local ductility in the vicinity of the crack tip is crucial to resisting FCP. It is this combination of high strength and relatively high ductility that allows the ED NC Ni–Co alloys (in this study) to demonstrate superior resistance to FCG.

Finally, it has been reported in the literature [4] that NC alloys do not experience significant levels of plasticity-induced crack closure, which is contrary to the findings of our present study (Fig. 8). The absence of reported crack closure is a combination of measurement resolution and instability of the microstructure ahead of the crack tip. In this case DIC was used to measure crack closure levels optically, which allows precise measurements of crack closure in NC materials. Additionally, the material is electrodeposited with low internal stress, which is combined with a stress relief heat treatment to further reduce the internal stress in the material [http://www.nicoform.com/files/upload/upload/23/Mechanical.pdf 2010]. This procedure stabilizes and equilibrates the microstructure, hence the grain structure is not susceptible to grain growth that may occur in other NC materials [15] during monotonic loading or especially during FCG testing, where regions of high stress accrue near the crack tip. It is possible that grain growth at the crack tip in other NC materials changes the local microstructure and stress state, which in turn does not allow for crack closure. In this study the stable microstructure based on a balance between an electro-deposition process that minimizes internal stress and a stress relief heat treatment does not result in grain growth during FCG, which adds to the resistance to FCG. Hence it is the combination of the strength and ductility achieved by alloying (as discussed further in Section 4.5), a stress relief

heat treatment, and grain stability which affords these ED NC Ni–Co alloys with superior damage tolerance and resistance to FCP.

4.3. Microstructure-based fatigue crack growth modeling

Classically the stable crack growth region II is not dependent on the microstructure of the material, although there is growing evidence in the literature that suggests that crack propagation in any region is a local phenomenon and, as such, it is dependent on the local microstructure of the material. McEvily and Boettner noted that the dislocations emitted from the crack tip would face obstacles based on the local microstructure of the material. These obstacles lead to dislocation pile-ups and perhaps a tendency of the dislocation to cross-slip, depending on the stacking fault energy of the material [35]. Yokobori et al. described the FCGR as proportional to the number of dislocations emitted from the crack tip [36]. Hence from this model crack propagation is a single rate process driven by the activation energy of dislocation nucleation at the crack tip. From this description the dislocation dynamics govern the crack mechanics, which would also depend on the local microstructure. The theoretical model of Tanaka et al. [37] suggested that crack growth is dependent on the grain size based on whether a slip band produced by the crack tip could transmit through a local GB and propagate into the adjacent grain, consistent with Zurek et al. [38]. Finally, Wu et al. presented an insightful model for local crack growth rate:

$$\frac{da}{dN} = \kappa(\gamma_f - \gamma_r)\left(\frac{\Delta K}{\sigma_y}\right)^2, \tag{6}$$

where γ_f and γ_r are the plastic strains during forward slip and reverse slip, respectively, produced from the motion of the dislocations once they are emitted from the crack tip and κ is a geometric factor of the slip plane relative to the crack [39]. Detailed in situ TEM images of the dislocations emitted from and positioned in front of the crack tip were observed by DeWald et al. [40].

To demonstrate these ideas of the role microstructure plays in FCP we summarize these mechanisms in Fig. 12. Fig. 12a–c displays our understanding of classical FCG [35] as a cyclic process of crack blunting and sharpening. Note that in Fig. 12a dislocations are emitted from the crack tip during forward loading, which leads to crack advancement and overall crack tip blunting, as indicated in Fig. 12b. During reverse loading (Fig. 12c) dislocations are emitted on a different slip system as the crack sharpens again, and the process repeats.

Now for the case of a NC material there is a higher density of GB due to the small sizes of the grains and a larger ratio of GB area to grain volume. In Fig. 12d dislocations are emitted from the crack tip during forward loading and these dislocations interact with a nearby GB (in this schematic a twin is shown due to the high fraction of twins within ED ND Ni–Co alloys). As the leading dislocation interacts with the twin boundary one of three outcomes may occur: (i) the dislocation cross-slips into the adjacent grain; (ii) the dislocation partially transmits into the adjacent grain resulting in a portion of the dislocation being incorporated in the boundary, i.e. a residual dislocation; (iii) the dislocation is blocked by the GB [41]. The exact outcome is dependent on the local stress state, applied loading direction, the material's stacking fault energy, and the geometry of the twin–dislocation system [42]. If a residual dislocation is left at the boundary the second dislocation that interacts at the boundary will have a higher activation energy for slip transmission. Eventually cases (ii) and (iii) lead to the twin boundary impeding dislocation motion representing a high barrier to dislocation transmission [43]. As a consequence of the twin boundaries being barriers to slip propagation a stress field arises due to the pile-up of dislocations, which prevents further dislocations from being emitted from the crack tip. In this case the twin serves as a mechanism to introduce slip irreversibilities during cyclic loading. This concept is covered in greater detail in Section 4.4. As a consequence, the crack cannot advance, as shown in Fig. 12e and f. During reverse loading the crack sharpens as dislocations are emitted on a different slip system. Note that in Fig. 12f the crack has not advanced compared with the advancing crack in Fig. 12c, which indicates an overall decrease in the FCGR.

Hence a high density of GB in a NC Ni–Co alloy leads to dislocation–GB interactions near the crack tip, slip irreversibilities, and, as a result, a slower FCGR, as depicted in Fig. 12. This is one of the mechanisms that leads to superior FCG resistance in ED NC Ni–Co alloys, although it does not explain why other NC materials experience significantly less resistance to FCG, as shown in Fig. 6. As previously discussed in Section 4. 2, the improved resistance to FCG of the ED NC Ni–Co alloys in this study is a combination of alloying, a stress relief heat treatment, and grain stability to achieve a balance of strength and ductility.

4.4. Slip irreversibility

As summarized in Fig. 12, the interaction of dislocations emitted from the crack tip with twins or GB in the local microstructure (in the vicinity of the crack tip) can lead to residual dislocations within the twin/GB. The result of this process is slip irreversibilities during fatigue loading, as the slip introduced during forward loading is not recovered during reverse loading due to activation of different slip systems and the presence of the twin/GB. It should be noted, however, that this is not the only source of slip irreversibilities during cyclic loading, and other mechanisms can produce such an effect, for instance annihilation of edge dislocations producing vacancies, cross-slipping of screw dislocations, shearing of precipitates, etc. For the case of this ED NC Ni–Co alloy the significant presence of twins/GB results in this mechanism being the dominant source of slip irreversibilities. Mughrabi quantified the cyc-

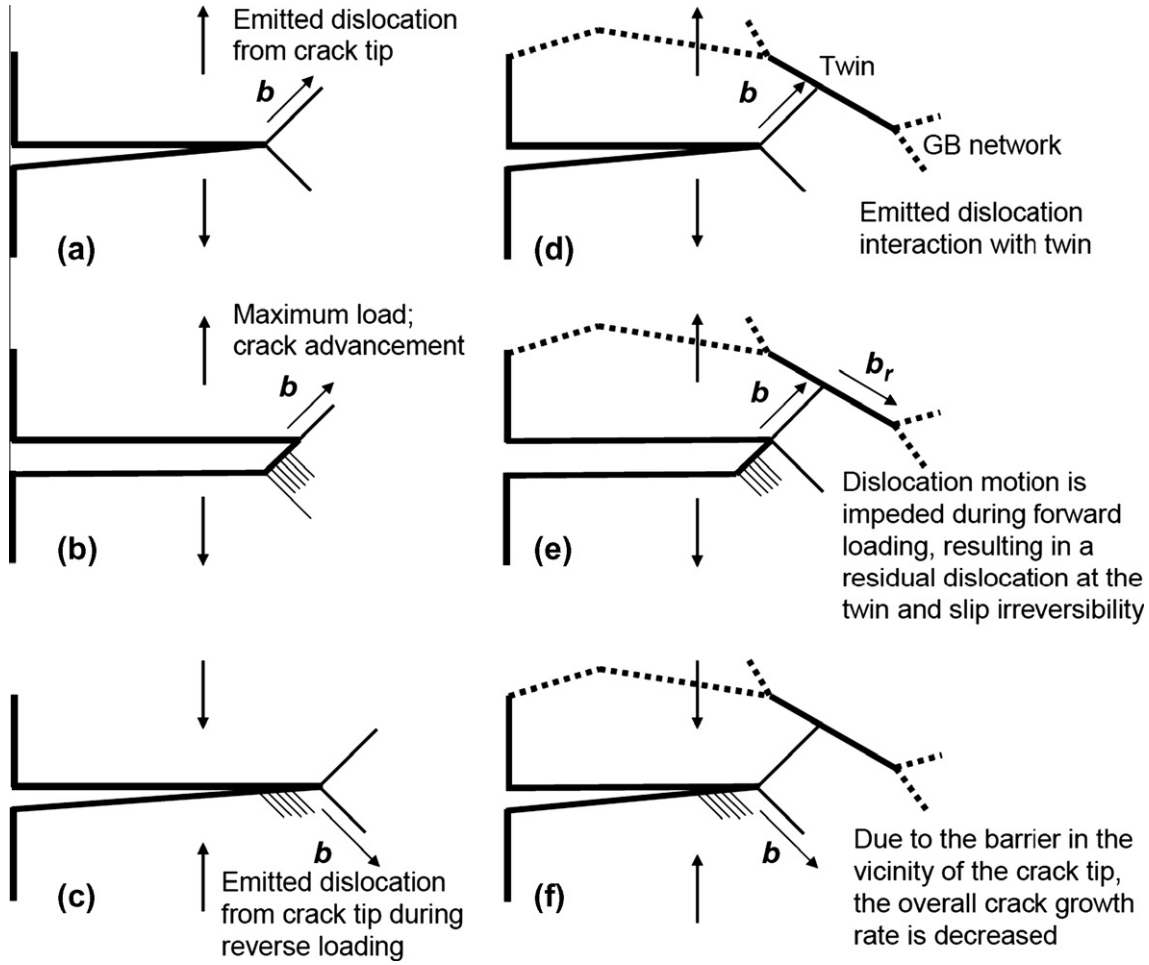

Fig. 12. (a–c) Classical FCG, which in this case is a function of fully reversible slip. (a) As the specimen is loaded dislocations are emitted from the crack tip on the active slip system during tensile loading. (b) The crack advances and the crack tip is blunted. (c) During reverse loading a different slip system is active, as dislocations are emitted. This process continues as the crack advances during alternating blunting and sharpening of the crack tip. (d–f) Impedance of FCG, as the microstructure leads to irreversible slip. (d) Dislocations are emitted from the crack tip and interact with a twin present in the microstructure. The dislocation is impeded during forward loading, resulting in a residual dislocation incorporated within the twin boundary. (f) During reverse loading dislocations are emitted, but note that the crack did not advance during the half cycle.

lic slip irreversibilities p, defined as the fraction of plastic shear strain that is microstructurally irreversible [44]. In this case p varies from 0, in the case of low loading amplitudes, to 1, in the case of high loading amplitudes and near stress concentrators such as the crack tip.

In order to gain a quantitative understanding of the slip irreversibilities on the continuum scale we measured strains within the plastic zone ahead of the crack tip during cyclic loading. DIC measured strains within the vicinity of the crack tip. In Fig. 7 we have quantified the monotonic plastic zone ahead of the crack tip as the material near the crack tip yields due to the high stresses produced by the crack. During cyclic loading the loading is reversed and, as a consequence, the plastic zone undergoes reverse yielding. As a result a reversed plastic zone exists ahead of a fatigue crack, where reverse plastic flow occurs within the classical monotonic plastic zone [45,46]. In fact, the radius of the cyclic plastic zone is theoretically a quarter of the radius of the monotonic plastic zone [45,46] for $R = 0$ without closure effects.

Hence the strain is measured within the cyclic plastic zone radius ahead of the crack tip at minimum load prior to the loading cycle (point A), at maximum load (point B), and at minimum load after completion of the current loading cycle (point C); these points are indicated in the hysteresis loops in Fig. 13e. At each point the strains measured by DIC are averaged within the cyclic plastic zone; $\Delta\varepsilon_{BA}$ indicates the strain accumulation during forward loading and $\Delta\varepsilon_{CA,ir}$ indicates the irreversible strain during the complete (forward and reverse) loading cycle. The displacement fields around the crack (allowing for the regression of the stress intensity factor value (Eq. (3))) along with a contour of the irreversible strains within the cyclic plastic zone are shown in Fig. 13. Within the inset to the figure are the values of $\Delta\varepsilon_{BA}$ and $\Delta\varepsilon_{CA,ir}$ and a schematic of the load versus time plot during a given cycle.

For the Ni–5.52% Co alloy the irreversible strain contours in the cyclic plastic zone ahead of the crack tip are shown for increasing crack size ($a/W = 0.26$, 0.50, and 0.68) in Fig. 13a–c, respectively. Note that, as expected,

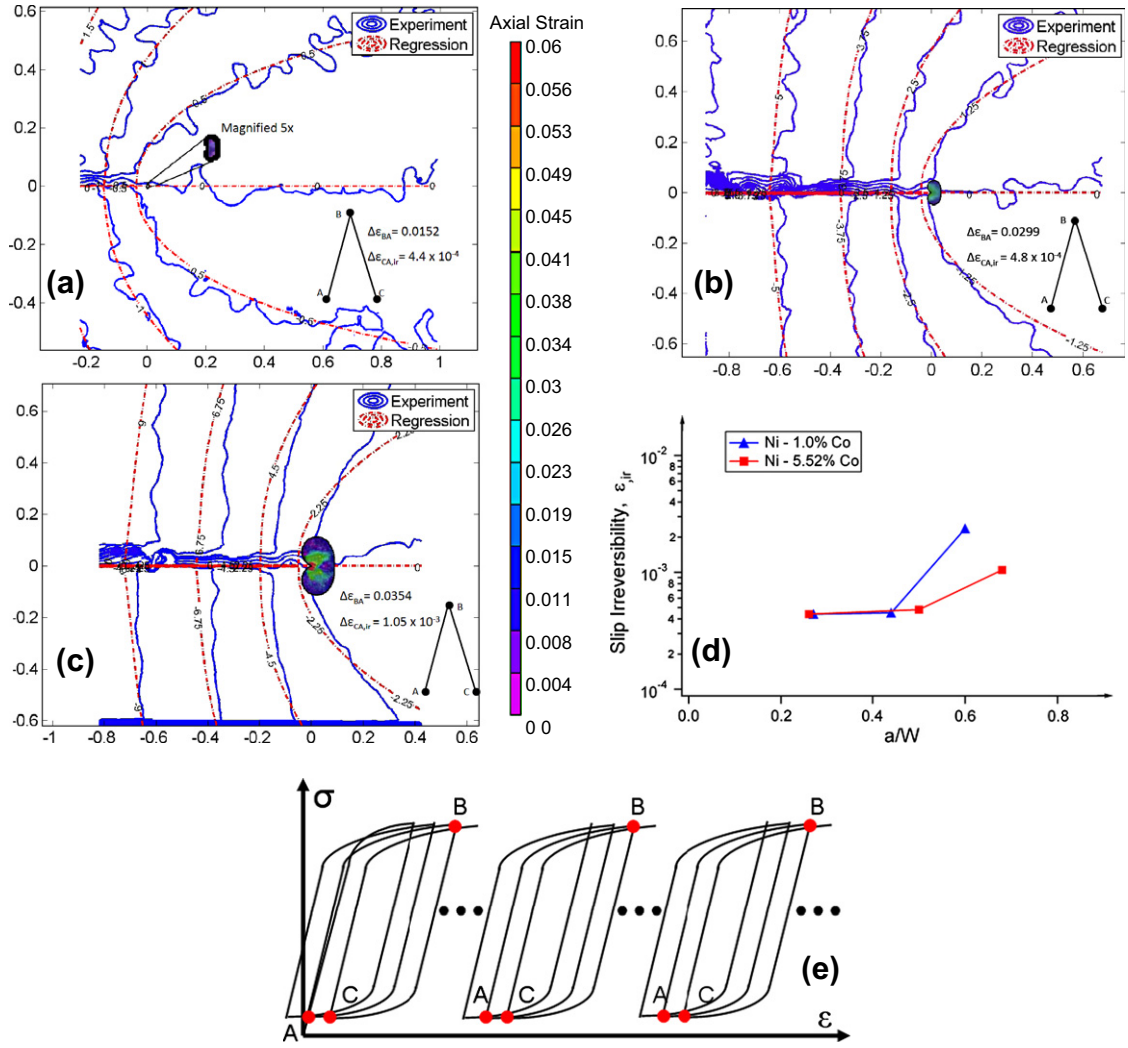

Fig. 13. Slip irreversibility in the ED NC Ni–5.52% Co material, shown as contour plots of the vertical displacements (μm), varies spatially (mm). Also shown is the plastic zone size ahead of the crack. Irreversible slip is measured as the difference in strain within the plastic zone ahead of the crack tip at point C compared with point A (see Fig. 13e). This gives the irreversible strain localized in the plastic zone from a single cycle at: (a) crack length $a/W = 0.26$, plastic zone radius $r_p = 10.5$ μm, maximum strain in plastic zone $\varepsilon_{max} = 0.0207$, maximum stress intensity factor $K_{max} = 9.16$ MPa × m$^{1/2}$, stress intensity factor when crack opens $K_{clos} = 2.33$ MPa × m$^{1/2}$, stress intensity factor range $\Delta K = 6.83$ MPa × m$^{1/2}$; (b) $a/W = 0.50$, $r_p = 37.0$ μm, $\varepsilon_{max} = 0.0491$, $K_{max} = 17.22$ MPa × m$^{1/2}$, $K_{clos} = 5.52$ MPa × m$^{1/2}$, $\Delta K = 11.7$ MPa × m$^{1/2}$; (c) $a/W = 0.68$, $r_p = 88.0$ μm, $\varepsilon_{max} = 0.0690$, $K_{max} = 26.44$ MPa × m$^{1/2}$, $K_{clos} = 8.12$ MPa × m$^{1/2}$, $\Delta K = 18.32$ MPa × m$^{1/2}$. (d) Slip irreversibility is shown for the given cycle, as the difference in average strain within the plastic zone ahead of the crack tip at point *C* vs. point A for two compositions of the Ni–Co material.

the radius of the cyclic plastic zone increases ($r_p = 10.5$, 37.0, and 88.0 μm) and the irreversibility strain accumulation during loading ($\Delta\varepsilon_{BA} = 0.0152$, 0.0299, and 0.0354) within this zone increases with increasing crack size. The average irreversible strain $\Delta\varepsilon_{CA,ir}$ within the cyclic plastic zone ahead of the crack tip (measured by DIC) is also plotted in Fig. 13d for Ni–1% and Ni–5.52% Co. The slip irreversibility increases with increasing crack size, i.e. higher stress intensity amplitudes, which is in agreement with Mughrabi, who stated that during cyclic loading higher values of slip irreversibility p should accompany higher applied loading amplitudes [44]. Finally, it is interesting to note that the measurement at the largest crack value indicates that the Ni–1% Co specimen had significantly higher slip irreversibility compared with Ni–5.52% Co. This slip irreversibility is linked to the resistance to FCG, as depicted in Fig. 12, and the lower Co concentration alloys experienced a greater resistance to FCG, as shown in Figs. 5 and 9.

4.5. Role of slip and twinning

As mentioned in Sections 4.1 and 4.2, the ED NC Ni–Co alloys displayed a high strength and strong hardening response in the monotonic tests and high resistance to FCG, i.e. damage tolerance. In this section we explain the deformation mechanisms present in this material which allow for these superior mechanical properties. TEM images of the ED NC Ni–1% Co alloy in the as-received condition, i.e. after electro-deposition and a stress relief

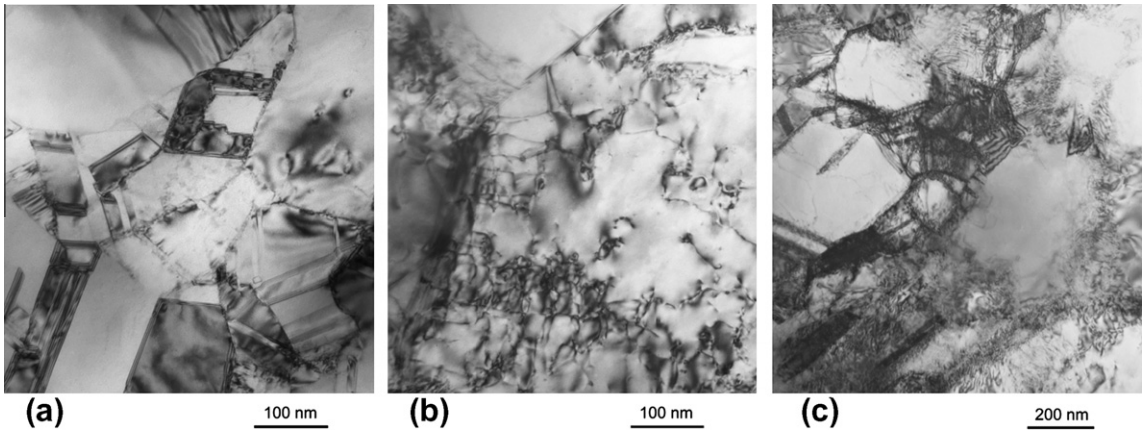

Fig. 14. TEM comparisons of dislocation density evolution within ED NC Ni–1% Co material: (a) as-received specimens, where dislocation densities are low and twinning is more prevalent (similar to Fig. 10a); (b and c) a specimen after failure during monotonic testing (see Fig. 4). The dislocation density increases as dislocation pile-ups are evident.

heat treatment, are shown in Figs. 10a and 14a. It is clear that a very large number of annealing twins are present within the material; as many as 40% of the boundaries are twin boundaries, as indicated by EBSD scans, although exact numbers cannot be reported due to the grain size approaching the limits of resolution of the EBSD system. However, it is apparent that in the as-received material annealing twins are prevalent and the material has a low density of dislocations, which suggests low internal stresses. TEM images of the ED NC Ni–1% Co alloy after failure during monotonic testing are shown in Fig. 14b and c (see Fig. 4). It is clear that an increase in dislocation density is experienced during monotonic loading, which suggests that a classical dislocation-based mechanism for plasticity,

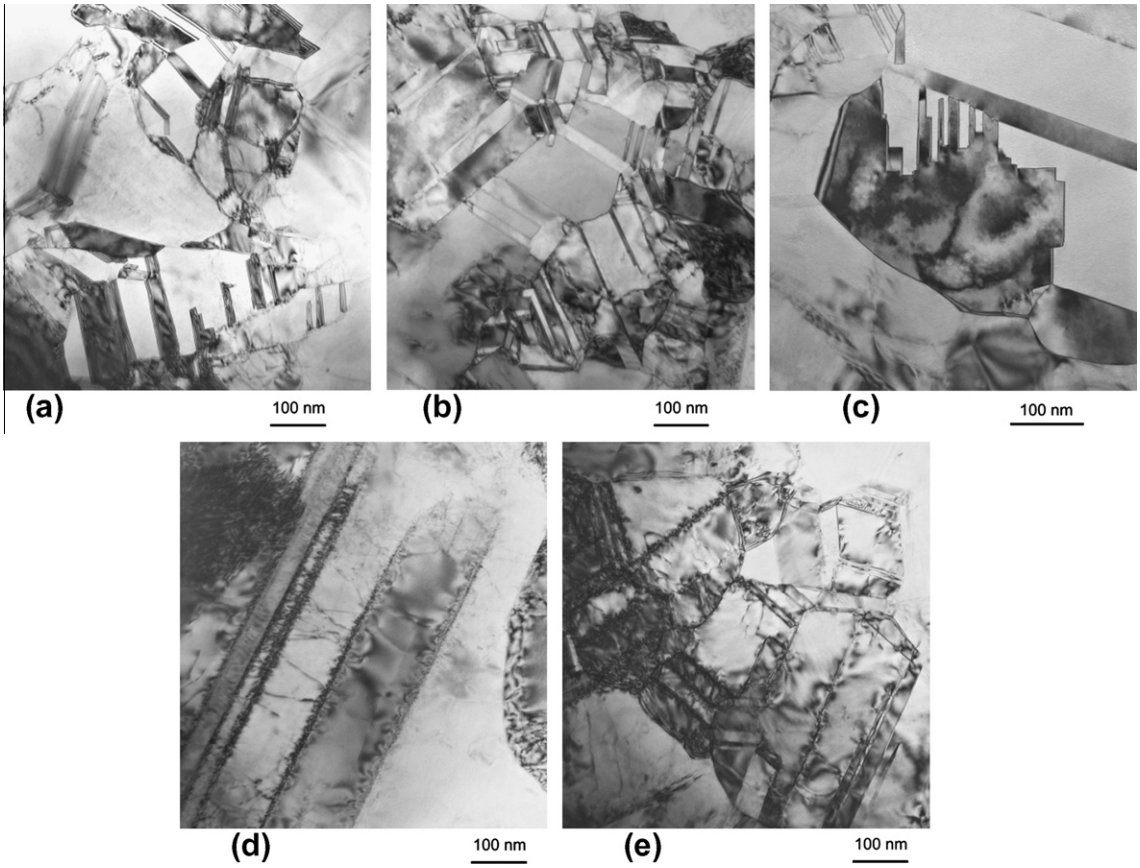

Fig. 15. TEM images of twinning within ED NC Ni–1% Co material: (a) as-received specimen displaying annealing twins; (b) FCG specimen displaying strong evidence of twinning; (c) FCG specimen in which more twins are present then dislocations; (d) monotonic specimen displaying slip–twin interaction; (e) monotonic specimen displaying twin–twin interaction.

for instance dislocation pile-ups, is present in this ED NC alloy, rather than GB sliding or other mechanisms suggested in the literature on NC materials.

Hence, annealing twins are present in this material arising from the ED process (Fig. 15a). In addition to this, the high stress state present at the crack tip results in twinning in the vicinity of the crack tip during cyclic loading and may even result in twinning at the crack tip, as dictated by the kinetics [47]. As such, we observe strong evidence of twinning near the crack tip after failure due to fatigue loading, as shown in Fig. 15b. In fact, in certain locations twinning is prevalent, with no signs of dislocations near the crack tip after fatigue failure (Fig. 15c).

Typically, in a binary material the addition of an alloying phase leads to solid solution strengthening, although this is not the case in this material. Both Co and Ni have nearly identical atomic radii (0.124 and 0.125 nm, respectively), electronic structures, and chemical potentials. Hence Co can substitute for Ni in the lattice and is not noticed as a point defect by moving dislocations. The main consequence of alloying Co in a Ni lattice is a reduction in the stacking fault energy [48], which results in greater strength and hardness. Lowering the stacking fault energy makes the material prone to deformation twinning, resulting in an increase in the hardening response of the material by slip–twin, twin–twin, and twin–GB interactions. Increasing the Co composition reduces the stacking fault energy of the material and increases the materials propensity to twin, although this trend is not the major difference in the response of the three alloys in our study with various concentrations of Co. At the lowest concentration of Co, Ni–1% Co, slip–twin (Fig. 15d), twin–twin (Fig. 15e), and twin–GB (Fig. 15e) are observed under monotonic loading. Hence, due to the prevalence of twinning, all three compositions experience twinning-related hardening during monotonic and cyclic loading at the crack tip. Further, the differences in monotonic strength and hardening behavior between the three alloys are dominated by grain size refinement and the concentration of LAGB, as discussed in Section 4.1.

In addition, since nanoscale twins provide a significant strengthening benefit within this ED NC Ni–Co alloy, the material is able to maintain its ductility. The twins are coherent with their surrounding matrix, thermally/mechanically stable, and are small in scale. Hence the twins present in our material fulfill the three requirements listed above, as stated by Lu et al. [23], and consequently promote strength while preserving ductility. It is this balance between strength and ductility that gives this ED NC Ni–Co alloy a greater resistance to FCP and superior damage tolerance properties.

5. Conclusions

Employing DIC measurements, monotonic and FCG experiments were used to study the mechanical properties of ED NC Ni–Co alloys. The aim of this work was to explain the superior resistance to FCP of these alloys through careful microstructure and mechanism characterization coupled with a model of cyclic slip irreversibilities. The significant contributions of this study are summarized as follows.

1. The ED NC Ni–Co alloys show high monotonic strength and the strength and hardening increased while the ductility decreased with increasing Co concentration. In this case Co acts to refine the grain size and increase the misorientation angle of the GB, and the combination acts as a strengthening mechanism in this material.
2. The addition of Co as an alloying element reduces the stacking fault energy of the material and as a result twinning is prevalent in Ni–Co. Annealing twins are present after electro-deposition, and consequently slip–twin, twin–twin, and twin–GB interactions are observed in the tensile and FCG specimens.
3. The NC Ni–Co alloys were electro-deposited with low internal stress, which was combined with a stress relief heat treatment to further reduce the internal stress in the material. This stabilizes the microstructure, such that grain growth is not experienced during testing. As a consequence, dislocation-mediated plasticity is the primary mechanism for deformation near the crack tip, which results in plasticity-induced crack closure.
4. This NC alloy results in a high density of GB per volume of material. At the crack tip there is competition between dislocation emission from the crack tip and crack advancement. Dislocations emitted from the crack tip interact with nearby GB resulting in slip irreversibilities that impede crack propagation, which is modeled in Section 4.3 and experimentally measured in Section 4.4.
5. The improved FCG resistance in this ED NC Ni–Co alloy is a combination of high strength ($\sigma_y > 500$ MPa) and ductility (local strains ~15% from DIC measurements). The most ductile material shows the highest resistance to FCG. Further, the nanoscale twins in this material (approximately 40% fraction of twins) provide an effective strengthening mechanism, while preserving the material's ductility.

Acknowledgements

Support for this work was provided primarily by Honeywell Aerospace Corporation and partially by the National Science Foundation (DMR 08-03270). The authors would like to thank Josh Kacher for his assistance with filtering the EBSD data and John Oyelakin for his assistance with the initial testing.

References

[1] Gleiter H. Acta Mater 2000;48:1.
[2] Meyers MA, Mishra A, Benson DJ. Prog Mater Sci 2006;51:427.
[3] Dao M, Lu L, Asaro RJ, De Hosson JTM, Ma E. Acta Mater 2007;55:4041.

[4] Padilla HA, Boyce BL. Exp Mech 2010;50:5.
[5] Kumar KS, Van Swygenhoven H, Suresh S. Acta Mater 2003;51:5743.
[6] Hanlon T, Kwon YN, Suresh S. Scripta Mater 2003;49:675.
[7] Kumar KS, Suresh S, Chisholm MF, Horton JA, Wang P. Acta Mater 2003;51:387.
[8] Xie J, Wu X, Hong Y. Scripta Mater 2007;57:5.
[9] Cheng S, Stoica AD, Wang XL, Wang GY, Choo H, Liaw PK. Scripta Mater 2007;57:217.
[10] Wei Q, Jia D, Ramesh KT, Ma E. Appl Phys Lett 2002;81:1240.
[11] Hanlon T, Tabachnikova ED, Suresh S. Int J Fatigue 2005;27:1147.
[12] Yang Y, Imasogie B, Fan GJ, Liaw PK, Soboyejo WO. Metall Mater Trans A 2008;39:1145.
[13] Moser B, Hanlon T, Kumar KS, Suresh S. Scripta Mater 2006;54:1151.
[14] Dalla Torre F, Spätig P, Schäublin R, Victoria M. Acta Mater 2005;53:2337.
[15] Kobayashi S, Kamata A, Watanabe T. Scripta Mater 2009;61:1032.
[16] Cavaliere P. Int J Fatigue 2009;31:1476.
[17] Rice JR, Thomson R. Philos Mag 1974;29:73.
[18] Ovid'ko IA, Sheinerman AG. Scripta Mater 2009;60:627.
[19] Ovid'ko IA, Sheinerman AG, Aifantis EC. Acta Mater 2008;56:2718.
[20] Wu BYC, Ferreira PJ, Schuh CA. Metall Mater Trans A 2005;36A:1927.
[21] Wang L, Gao Y, Xue Q, Liu H, Xu T. Appl Surf Sci 2005;242:326.
[22] Bansal S, Saxena A, Hartwig T, Tummala RR. Fatigue and fracture behavior of nanocrystalline copper and nickel. In: 11th International conference on fracture, Turin; 2005.
[23] Lu K, Lu L, Suresh S. Science 2009;324:349.
[24] Sutton MA, Wolters WJ, Peters WH, Ranson WF, McNeill SR. Image Vis Comput 1983;1:133.
[25] Carroll J, Efstathiou C, Lambros J, Sehitoglu H, Hauber B, Spottswood S, et al. Eng Fract Mech 2009;76:2384.
[26] Peralta P, Choi SH, Gee J. Int J Plast 2007;23:1763.
[27] Hertzberg RW. Deformation and fracture mechanics of engineering materials. New York: Wiley; 1989.
[28] Pook LP. In: Corten HT, editor. Stress analysis and growth of cracks; 1972.
[29] Westergaard HM. Trans Am Soc Mech Eng J Appl Mech 1939; 6:49.
[30] Elber W. ASTM special technical publication. West Conshohocken (PA): ASTM; 1971. p. 230.
[31] Christensen RH. Appl Mater Res 1963;2:207.
[32] Elber W. Eng Fract Mech 1970;2:37.
[33] Zhang ZF, Wang ZG. Acta Mater 2003;51:347.
[34] Canadinc D, Biyikli E, Niendorf T, Maier HJ. Adv Eng Mater 2011;13:281.
[35] McEvily JAJ, Boettner RC. Acta Metall 1963;11:725.
[36] Yokobori T, Yokobori Jr AT, Kamei A. Int J Fract 1975;11:781.
[37] Tanaka K, Nakai Y, Yamashita M. Int J Fract 1981;17:519.
[38] Zurek AK, James MR, Morris WL. Metall Trans A 1983;14A: 1697.
[39] Wu XJ, Koul AK, Krausz AS. Metall Trans A 1993;24A:1373.
[40] Dewald DK, Lee TC, Robertson IM, Birnbaum HK. Scr Metall 1989;23:1307.
[41] Lee TC, Robertson IM, Birnbaum HK. Scr Metall 1989;23:799.
[42] Ezaz T, Sangid MD, Sehitoglu H. Philos Mag 2011;91:1464.
[43] Sangid MD, Ezaz T, Sehitoglu H, Robertson IM. Acta Mater 2011;59:283.
[44] Mughrabi H. Metall Mater Trans B 2009;40:431.
[45] McClintock FA. In: Drucker DC, Gilman JJ, editors. Fracture of solids, vol. 20. New York: Wiley; 1963. p. 65.
[46] Rice JR. In: Grosskreutz J, editor. Fatigue crack propagation, vol. 415. Philadelphia: ASTM STP; 1967. p. 247.
[47] Warner DH, Curtin WA, Qu S. Nat Mater 2007;6:876.
[48] Beeston BEP, Dillamore IL, Smallman RE. Metal Sci J 1968;2:12.